Check for updates

#### RESEARCH ARTICLE

# Impact of tissue sample preparation methods on myelin-sensitive quantitative MR imaging

Amaya Murguia<sup>1</sup> | Scott D. Swanson<sup>2,3</sup> | Ulrich Scheven<sup>4</sup> | Andrea Jacobson<sup>5</sup> Jon-Fredrik Nielsen<sup>1,2,5</sup> | Jeffrey A. Fessler<sup>1,2,5</sup> | Navid Seraji-Bozorgzad<sup>6</sup>

- <sup>2</sup>Department of Radiology, University of Michigan, Ann Arbor, Michigan, USA
- <sup>3</sup>Department of Biophysics, University of Michigan, Ann Arbor, Michigan, USA
- <sup>4</sup>Department of Mechanical Engineering, University of Michigan, Ann Arbor, Michigan, USA
- <sup>5</sup>Department of Biomedical Engineering, University of Michigan, Ann Arbor, Michigan, USA
- <sup>6</sup>Department of Neurology, University of Michigan, Ann Arbor, Michigan, USA

#### Correspondence

Amaya Murguia, Functional MRI Laboratory, University of Michigan, 2360 Bonisteel Blvd., Ann Arbor, MI 48109, USA.

Email: amurguia@umich.edu

# **Funding information**

National Institute on Aging, Grant/Award Number: P30AG072931-03S1

#### **Abstract**

**Purpose:** Validation of quantitative MRI (qMRI) parameters with histology is often done with ex vivo fixed tissue samples. Freezing is another common form of tissue preservation, but the effects of freezing and thawing tissue on myelin-sensitive quantitative MRI parameters and their correlation with histology require further analysis.

Methods: Myelin water imaging, off-resonance RF saturation magnetization transfer (MT), and selective inversion recovery MT MRI experiments were conducted on 14 fresh, thawed, and fixed sheep brain tissue samples to calculate various surrogate measures of myelin content. These measures were compared with luxol fast blue (LFB) histological stain results.

**Results:** Fresh, thawed, and fixed tissue qMRI values correlated well with LFB. Thawed and fixed tissue exhibited modest increases, between 3% and 32%, for most qMRI parameter values compared to fresh. Histology results showed that thawed samples did not lose tissue integrity from the freezing process.

**Conclusion:** Freezing is a reasonable alternative tissue preservation method to fixation for use in qMRI analysis, but may differentially affect qMRI parameter values in regions with varying myelin content.

#### KEYWORDS

bi-exponential T<sub>1</sub> mapping, luxol fast blue histology, myelin water imaging (MWI), quantitative magnetization transfer (qMT), quantitative MRI, tissue preparation

#### 1 INTRODUCTION

Quantitative MRI (qMRI) has been proposed as a more specific marker of disease pathology than MRI contrast images, and many qMRI methods have been developed to provide quantitative myelin-sensitive metrics. Many prior qMRI studies have focused specifically on myelin-sensitive qMRI, as demyelination is the cause of many diseases, such as multiple sclerosis,<sup>2</sup> and is involved in many others, such as Alzheimer's disease.3 Quantitative MRI parameters are often validated with histology in fixed tissue samples<sup>4–9</sup>;

This is an open access article under the terms of the Creative Commons Attribution-NonCommercial-NoDerivs License, which permits use and distribution in any medium, provided the original work is properly cited, the use is non-commercial and no modifications or adaptations are made.

<sup>&</sup>lt;sup>1</sup>Department of Electrical Engineering and Computer Science, University of Michigan, Ann Arbor, Michigan, USA

however, fixation can alter MR tissue properties, including myelin-sensitive properties, <sup>10</sup> and even immunohistochemistry and histological findings. 11 Freezing is another method for post-mortem storage that preserves nucleic acid components for genetic analysis on DNA, but a potential concern when using thawed tissue is the effect of the freeze-thaw cycle on cellular integrity, as ice crystals formed during freezing, cold storage, and thawing may destroy tissue components. 12,13 This study compared the effects of both tissue preparation techniques, freezing and fixation, on myelin-sensitive qMRI parameters using three methods: myelin water imaging, off-resonance RF saturation magnetization transfer (MT) imaging, and selective inversion recovery MT imaging. These methods were chosen since they encompass fundamental contrast mechanisms that are widely accepted to be myelin-sensitive.

Myelin water imaging (MWI) is a common method for analyzing tissue myelin content and is based on the principle that water molecules within the myelin sheath interact more frequently with membrane molecules leading to shorter T2 times than axonal or extracellular water. The MRI signal is a superposition of water signals in different compartments, leading to multi-exponential decay.<sup>2</sup> The standard MWI experiment collects multiple spin echoes and fits the curve with non-negative least squares regression to determine the relative signal contribution from each T<sub>2</sub> component. T<sub>2</sub> spectra typically have two peaks corresponding to myelin water and free water. 14,15 The fraction of the signal below a T2 cutoff between the two peaks is defined as the myelin water fraction (MWF), which has been histologically validated and accepted as a measure of myelin content. 4-7,16,17 However, it has been validated with fixed tissue, and fixation has been shown to decrease T2 values18-22 and increase MWF.10,16,23 A study found that freezing and thawing tissue decreased water content, but did not significantly affect T<sub>2</sub>.<sup>24</sup> Another found that fresh and thawed samples exhibited similar signal behavior when imaged with ultrashort-T<sub>2</sub> techniques, but the thawed samples had consistently lower signal magnitudes than the fresh.<sup>25</sup> The effects of freezing and thawing tissue on MWF have not been widely studied.

Magnetization transfer (MT) is another common technique used in white matter (WM) imaging studies.  $^{26-28}$  MT in myelin is dominated by exchange of water and macromolecular protons. The macromolecular protons have  $T_2$  times of order  $10~\mu s$  and decay too fast to be observed using typical MRI sequences. Conventional MT imaging applies an MT preparation pulse far off-resonance from the water signal, directly saturating the macromolecular proton longitudinal magnetization. Proton exchange carries the depleted membrane magnetization to the water molecules,

indirectly saturating the free (MR-visible) water magnetization. The semi-quantitative magnetization transfer ratio (MTR), the difference between the images obtained with and without the preparation pulse, normalized by the image without the preparation pulse, <sup>29</sup> has been previously validated in tissue samples for its sensitivity to myelin content. <sup>8,9</sup> Images acquired after applying preparation pulses at multiple RF power levels and off-resonance frequencies are fit to a quantitative MT (qMT) signal model to calculate the fractional size of the bound pool (F), <sup>30,31</sup> which is another accepted measure of myelin content. <sup>32–34</sup> Fixation increases the effect of MT, <sup>10,22,35,36</sup> and freezing can increase MTR. <sup>24</sup>

Quantitative  $T_1$  mapping has also been used to study myelination<sup>37–40</sup> and perform qMT analysis,<sup>41–45</sup> where the observed signal recovery is driven by MT. An inversion pulse selectively inverts water magnetization but not macromolecular proton magnetization. After this pulse, magnetization quickly flows into the inverted water pool from the solid pool.<sup>46,47</sup> Inversion recovery data are fit to a bi-exponential model to calculate the long and short  $T_1$  components and their corresponding amplitudes.<sup>37,46</sup> These parameters can be used to calculate the ratio of the sizes of the macromolecular and free water proton pools (F) as well.<sup>41,43,45</sup> Similar to  $T_2$  relaxation, fixation decreases the  $T_1$  value of water,<sup>18–22</sup> and one study found that freezing tissue also decreases  $T_1$ .<sup>24</sup>

In this study, we extended preliminary work 48,49 where we conducted MWI and qMT experiments and luxol fast blue (LFB) histological staining on fresh, thawed, and fixed sheep brain tissue samples to analyze the effects of formalin fixation and freezing on qMRI measures of myelin content. We compared these qMRI parameter values across tissue conditions and correlated them with LFB values.

### 2 | METHODS

# 2.1 | Samples and equipment

Our process and procedures were compliant with and conducted with the approval of our university's Institutional Animal Care and Use Committee (IACUC). Seven unfixed, unfrozen ex vivo whole sheep brains were obtained from Nebraska Scientific (Omaha, NE, USA). Immediately after death, the tissues were transferred to a 4°C refrigerator. The time between death and brain extraction was seven days, and the whole brains were shipped to us five days after extraction, with a transit time of 12 h on ice. We sectioned the specimens (see Figure S1 for an illustration) and placed them in the refrigerator at 4°C for up to one day. The total time between death and scanning was 12–13

days. The whole-brain specimens were cut into  $\sim$ 13-mm thick coronal sections; sections at the level of the caudate nucleus were placed into histology cassettes of size  $40 \times 26 \times 13$  mm for MR scanning (N=13). One specimen was cut as a parasagittal section of the same thickness, resulting in 14 total samples. All samples allowed for examination of a variety of tissue types, including WM structures such as the corpus callosum, fornix, cortical white matter, and internal capsule, as well as cortical and subcortical gray matter (GM).

Each cassette was submerged in Fluorinert FC-770 (3M, St. Paul, MN, USA) to minimize B<sub>0</sub> field inhomogeneity. All specimens were imaged fresh with our entire imaging protocol. Following fresh sample data collection, seven cassettes were placed in a -80°C freezer. After about three weeks, the frozen samples were thawed for 48 h at 4°C before their second round of imaging with the same protocol. The other seven cassettes were placed directly in 10% formalin for 36 h after the fresh scan, washed in normal saline solution for 12 h, and scanned again with the same protocol. 36 h of fixation gives enough time for protein cross-linking and tissue preservation without a significant effect on any subsequent immunohistological methods. This time frame was chosen after discussion with neuropathologists at the Unit for Laboratory Animal Medicine (ULAM) Pathology Core, and proved to be sufficient based on subsequent histological analysis. All samples were placed in 10% formalin and stored at room temperature before histological analysis.

For imaging, the samples were placed in a 40 mm Millipede quadrature coil and inserted into a 7.0 Tesla NMR/MRI scanner (Varian/Agilent, Walnut Creek, CA, USA) with 40 mT/m gradients with a 115-mm inner diameter. The studies were conducted below room temperature at  $\sim 15^{\circ}$ C-20°C to ensure that the fresh and freshly thawed samples did not decay during the scanning process. Two rounds of  $B_0$  shimming were performed voxel-wise across the sample using a 3D gradient echo shimming routine. Three of the 14 samples were scanned with a 40 mm saddle coil (Morris Inc., ON, CAN) due to equipment availability; statistical analyses in Section 2.5 accounted for this difference.

# 2.2 | Myelin water imaging

Multi-echo spin echo (MESE) data were collected using a multi-echo multi-slice (MEMS) 2D slice-selective sequence with the following parameters: TR = 4000 ms, 64 echoes, echo spacing = 5 ms, matrix size =  $128 \times 128$ , and Carr-Purcell-Meiboom-Gill (CPMG) phase cycling (custom or default Varian sequence) with two signal averages. The excitation pulse (90° flip angle) was a 5-lobe sinc

pulse with a 1000  $\mu$ s pulse duration and 5944 Hz bandwidth. The refocusing pulse (180° flip angle) was also a five-lobe sinc pulse with an 8000  $\mu$ s width and 5877.5 Hz bandwidth. Data were acquired for five interleaved slices with thickness = 2 mm, slice gap = 0 mm, field of view =  $35 \times 35 \text{ mm}^2$ , in-plane resolution =  $273 \times 273 \mu\text{m}^2$ . The total scan time per sample was 17 min.

The MESE data were analyzed voxel-wise with regularized non-negative least squares (NNLS) regression using the extended phase graph (EPG) formalism to estimate a T<sub>2</sub> spectrum for each voxel.<sup>14</sup> The fitting process used 50 T<sub>2</sub> values log spaced from 5 to 1000 ms and a regularization parameter of 0.001 to jointly estimate a B<sub>1</sub> field inhomogeneity scaling factor for each voxel using 16 values linearly spaced values from 0.7-1.1; this B<sub>1</sub> map was then fixed and the T<sub>2</sub> spectrum was estimated with 500 T<sub>2</sub> values log spaced from 5 to 1000 ms and the same regularization parameter.<sup>50,51</sup> The myelin water fraction (MWF) calculation used a cutoff value of 20 ms.5 The MWF was calculated for each voxel as the sum of the amplitudes of the points in the T<sub>2</sub> spectrum up to the cutoff divided by the sum of the amplitudes of the entire spectrum. These values were used to generate a MWF map. We conducted the NNLS fitting with the NNLS package (https://github .com/rdeits/NNLS.jl) in the Julia programming language version 1.8.5 (https://julialang.org). Figure 1 illustrates the steps in the MESE data processing pipeline for a representative fresh sample.

# 2.3 | Quantitative magnetization transfer

Quantitative MT imaging was conducted using two different sequences and processing methods. The first was steady-state off-resonance RF saturation and MT parameter fitting according to the binary spin-bath model,  $^{30,31}$  and the second was transient recovery of selectively inverted water proton magnetization and bi-exponential  $T_1$  mapping.  $^{41}$ 

# 2.3.1 | Off-resonance RF saturation

Single-slice MT data were collected via a 2D gradient echo, slice-selective sequence with the following parameters: TR = 120 ms, TE = 3 ms, flip angle = 20°, and matrix size = 128 × 128. The excitation pulse (90° flip angle) was a 5-lobe sinc pulse with a 1000  $\mu$ s width. The MT preparation pulses consisted of a train of 20 Gaussian pulses of duration 1 ms, bandwidth 796 Hz, and duty cycle ~ 16.7% at 25 off-resonance frequencies from -60 to +60 kHz at 5 kHz increments and four RF B<sub>1</sub> RMS amplitudes at about 17.6,

.522254, 2025. 5, Downloaded from https://onlinelibrary.wiley.com/doi/10.1002/mrm.30623 by University Of Michigan Library, Wiley Online Library on [28/08/2025]. See the Terms and Conditions (https://onlinelibrary.wiley

ions) on Wiley Online Library for rules of use; OA articles are governed by the applicable Creative Commons

Myelin water imaging analysis for a representative fresh sample.<sup>48</sup> (A) Spin echo image (TE = 5 ms) marked with WM (blue) and GM ROIs (red). (B) Observed (dotted curve) and fitted (smooth curve) signal decay curves versus echo time for one WM voxel and one GM voxel in the labeled ROI. (C) Average T2 spectra for the WM and GM ROIs. (D) MWF map, calculated using a 20 ms T2 cutoff (indicated in (C)). The MWF map is taken as a surrogate measure of myelin content.

8.8, 4.4, and 2.2  $\mu$ T with flip angles of 8960°, 4480°, 2240°, and 1120°, respectively. The slice thickness = 2mm, field of view =  $35 \times 35$  mm<sup>2</sup>, and in-plane resolution =  $273 \times 273$  $\mu$ m<sup>2</sup>. The total scan time per sample was 26 min.

The magnetization transfer ratio (MTR) was calculated as  $\frac{S_0-S_+}{S_0}$ , where  $S_+$  is an image obtained with an MT preparation pulse at 10 kHz and S<sub>0</sub> is the image obtained at 60 kHz off-resonance. The reported MTR is the average of the MTR maps at +10 and -10 kHz off-resonance and B<sub>1</sub> field

A nonlinear parametric voxel-wise fit using the binary spin-bath MT model was performed on the MT data. 30,31,52 The two-pool model consists of a free water pool, M<sub>f</sub>, with a Lorentzian lineshape and a macromolecular proton pool, M<sub>m</sub>, with a super-Lorentzian lineshape.<sup>53–55</sup> For each voxel, three parameters were fixed. The long T<sub>2</sub> value of the free water pool, T2.f, was assigned a value from a weighted average of the MWI T2 spectrum data for all T2 values beyond the 20 ms cutoff. R1.f was set to  $0.33 \text{ s}^{-1}$ , the approximate  $R_1$  of water at 7T in the absence of magnetization transfer, and  $R_{1,m}$  was set to 1 s<sup>-1</sup>, as done in prior studies. 31,46,56 The remaining parameters were estimated: the T<sub>2</sub> value of the macromolecular pool T<sub>2,m</sub>, the cross-relaxation rate of exchange between the pools R, the ratio of macromolecular to total free water protons  $F_{sat} = \frac{M_m}{M_f}$ , and the chemical shift of the macromolecular pool,  $\Delta_{cs,m}$ ; see Section S2 in the Supporting Information for further details about the signal model. Corrections for B<sub>0</sub> and B<sub>1</sub> inhomogeneities were also included in the model fitting using acquired maps. We conducted nonlinear fits with MATLAB R2023a (Math-Works, Natick, MA, USA). Figure 2 illustrates the steps in the MT data processing pipeline for a representative fresh sample.

#### 2.3.2 Selective inversion recovery

Inversion recovery data were collected using a 2D slice selective inversion recovery (SIR) scan with a ramp-sampled spin-echo echo-planar imaging (EPI) readout at 21 inversion times (TI) logarithmically spaced from 10 ms to 5 s with the following parameters: TR = 8000ms, TE = 36 ms, and matrix size =  $64 \times 64$ . The excitation pulse (90° flip angle) was a 5-lobe sinc pulse with a 2000 us width. The refocusing pulse (180° flip angle) was also a 5-lobe sinc pulse with a 1600  $\mu$ s width. The inversion pulse (180° flip angle) was a hyperbolic secant (HS) adiabatic full passage (AFP) pulse<sup>57</sup> with a 4000  $\mu$ s width and a power of 51  $\mu$ T. A B<sub>0</sub> map, which was needed for EPI distortion correction, was acquired separately using a 2D gradient echo slice-selective sequence with multiple TE values at 4, 6, 8, and 10 ms, TR = 100 ms, flip angle =  $20^{\circ}$ , and matrix size = 128 × 128. Data were acquired for five interleaved slices with thickness = 2 mm, slice gap = 0 mm, field of view =  $35 \times 35 \text{ mm}^2$ , and in-plane resolution =  $547 \times 547 \mu \text{m}^2$ . The total scan time per sample was 6 min for the EPI IR scan and 1 min for the  $B_0$  mapping scan.

The IR EPI distorted images were unwarped, upsampled to a  $128 \times 128$  matrix size, and registered to the MESE data.58 Then, a bi-exponential two-pool model fit was performed on the IR data using nonlinear least squares (NLLS).<sup>41</sup> Five parameters were estimated voxel-wise: the short and long T<sub>1</sub> values corresponding to the fast and slow recovery rates, their corresponding amplitudes afast and a<sub>slow</sub>, and a B<sub>1</sub> field inhomogeneity scaling factor. The ratio of macromolecular to free water protons,  $F_{SIR} = \frac{M_m}{M_c}$ , <sup>41</sup> was calculated as 2× the fast relaxing component amplitude a<sub>fast</sub> 41 assuming full saturation of the macromolecular pool by the hyperbolic secant pulse; see Sections S3 and S4 and

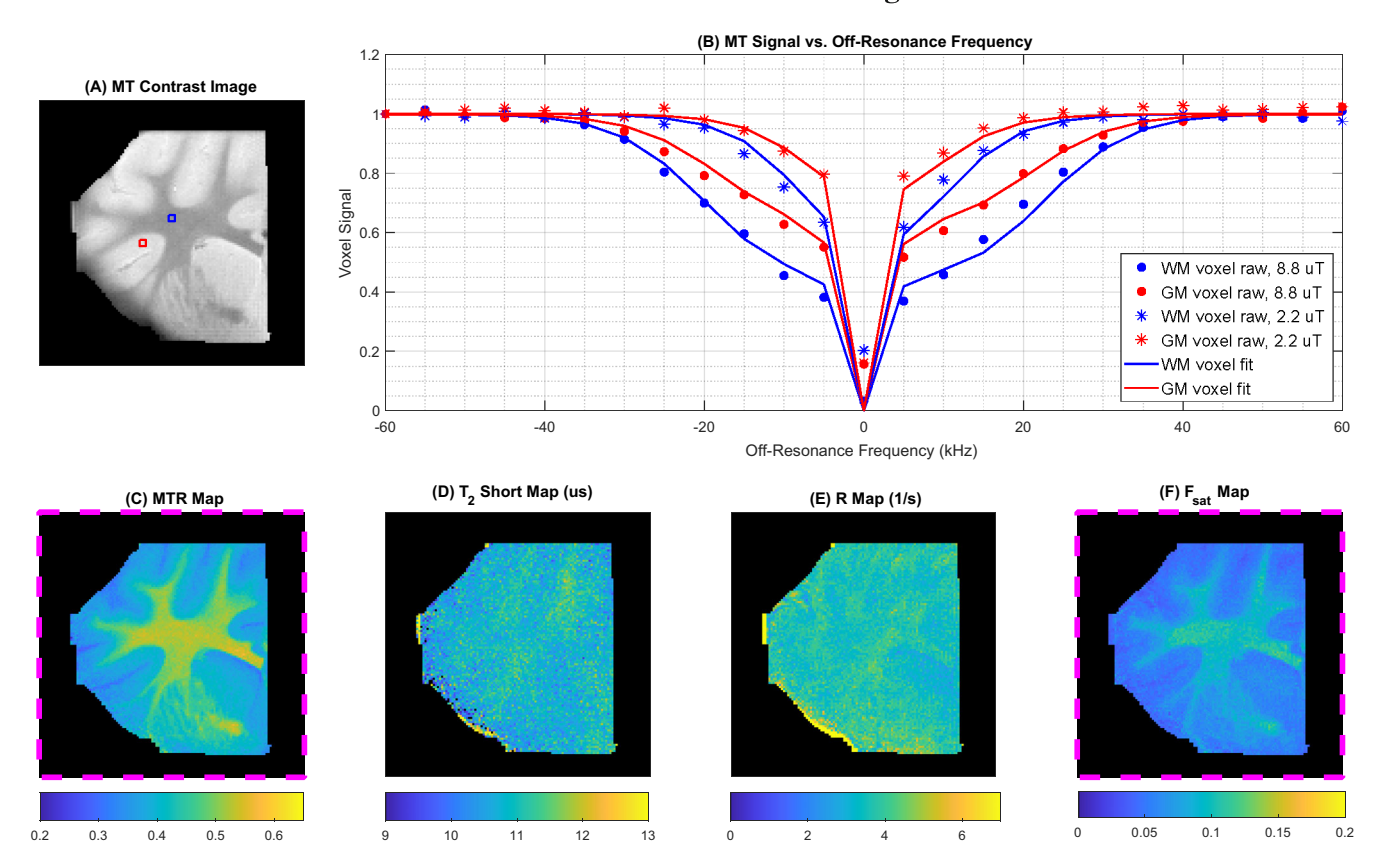


FIGURE 2 Saturation-based MT analysis for a representative fresh sample. (A) MT contrast image at 10 kHz off-resonance and second highest power level (8.8  $\mu$ T) marked with WM (blue) and GM (red) ROIs. (B) Observed and fitted normalized signal curves versus off-resonance frequencies from -60 to 60 kHz for one WM voxel and one GM voxel in the ROI for two of the four power levels (8.8 and 2.2  $\mu$ T). (C) MTR map calculated with the average of the -10 and 10 kHz images and 8.8  $\mu$ T power level. (D) Map of the estimated short T<sub>2</sub> value corresponding to the macromolecular pool in  $\mu$ s for each voxel. (E) Map of the estimated rate constant R characterizing the exchange rate between the two pools in seconds for each voxel. (F) Map of the ratio of macromolecular to free water protons F<sub>sat</sub>. Maps outlined in pink (C, F) are taken as surrogate measures of myelin content. The short T<sub>2</sub> and R maps have low WM/GM contrast compared to prior studies this may be due to temperature effects.

Figure S3 for further details. This quantity is the same as the definition of  $F_{sat} = \frac{M_m}{M_f}$  in Section 2.3.1,<sup>59,60</sup> and is also called the pool size ratio (PSR) in other papers.<sup>41,43,59</sup> We conducted the nonlinear fit with MATLAB R2023a (Math-Works, Natick, MA, USA). Figure 3 illustrates the steps in the IR data processing pipeline for a representative fresh sample.

# 2.4 | Histological analysis

After imaging, all samples were immediately placed in 10% formalin to undergo fixation. After fixation, the tissue was bisected along the coronal plane with a razor to facilitate paraffin embedding. The top half, based on orientation in the magnet, was stored for further studies, and the other half underwent paraffin embedding followed by microtomy to obtain a 5  $\mu m$  slice corresponding to the center of the original sample. The sample then underwent luxol

fast blue (LFB) staining for myelin visualization and cresyl violet (CV) counterstaining for cell nuclei visualization; Figure S2 includes further details. Then they were scanned with a resolution of 0.5  $\mu$ m/pixel using a Vectra Polaris brightfield whole-slide scanner (Akoya Biosciences, Marlborough, MA, USA). We used the blue channel minus the red channel as a measure of LFB-CV optical density (referred to as LFB in the following text).

# 2.5 | ROI and statistical analysis

We used Freeview (https://github.com/freesurfer/freesurfer/tree/fs-7.2/freeview) to label the histology and two corresponding MR center slice images for both tissue conditions (fresh/thawed and fresh/fixed). The images were labeled with WM and GM regions of interest (ROIs), which were done by manually looking for prominent anatomical WM and GM features in both the MR contrast and

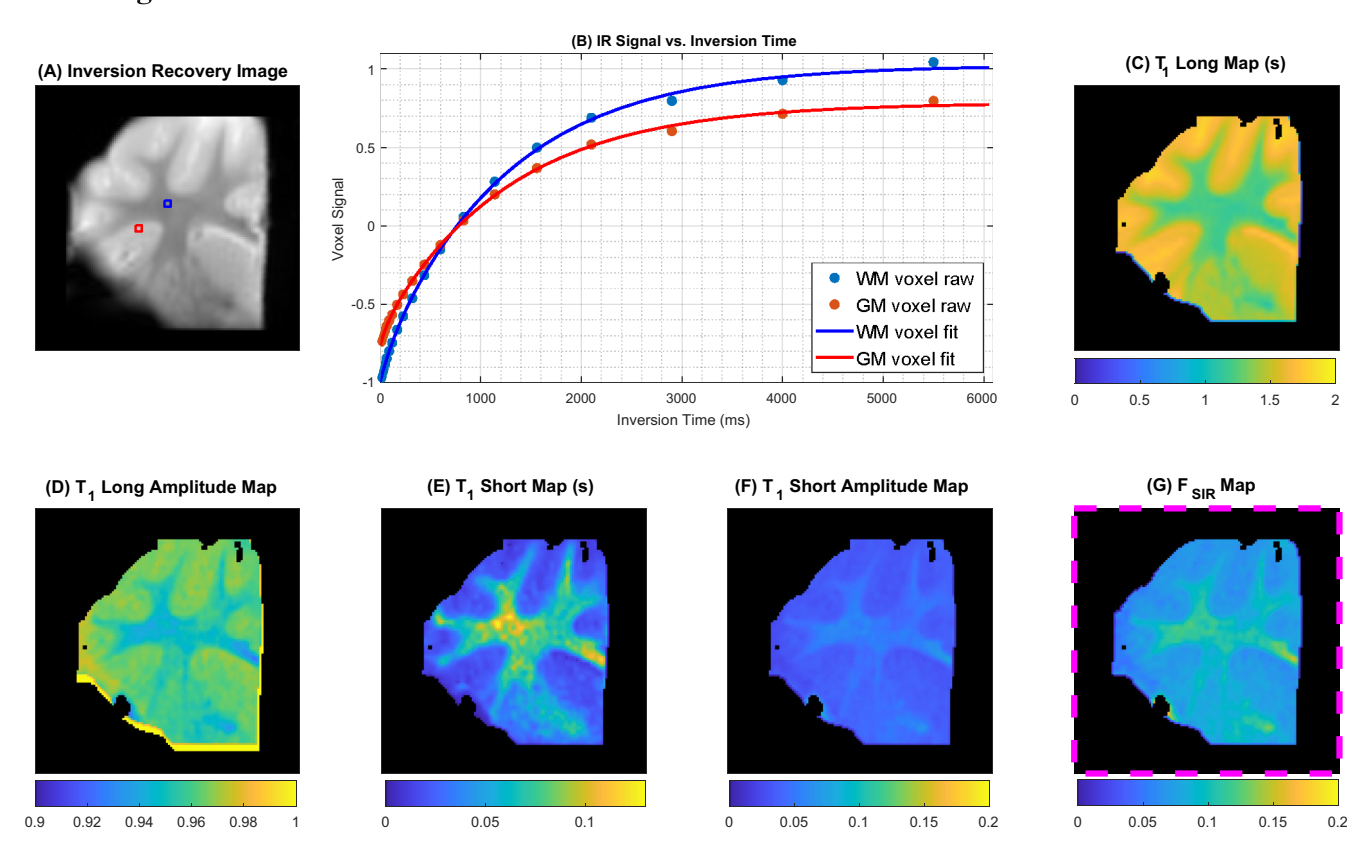


**FIGURE** 3 Selective inversion recovery bi-exponential analysis for a representative fresh sample. <sup>48</sup> (A) IR image (TI = 10 ms) marked with WM (blue) and GM (red) ROIs. (B) Observed and fitted signal recovery curves versus inversion time for one WM voxel and one GM voxel in the ROI. (C) Map of the estimated long  $T_1$  value for each voxel. (D) Normalized corresponding signal amplitude for the long  $T_1$  component ( $a_{slow}$ ) for each voxel. (E) Map of the estimated short  $T_1$  value for each voxel. (F) Normalized corresponding signal amplitude for the short  $T_1$  component ( $a_{fast}$ ) for each voxel. (G)  $F_{SIR}$  map outlined in pink is taken as a surrogate measure of myelin content.

histology images. The ROIs were selected using a  $4 \times 4$  region in the MR images, corresponding to an area of about 1 mm<sup>2</sup>. The histology ROIs were selected from an  $8 \times 8$  region on a downsampled image, corresponding to approximately a 0.25–1 mm<sup>2</sup> range of tissue. Figure 4 shows a representative sample with corresponding MR-and histology-labeled ROIs.

All statistical analysis was done using R version 4.4.1 (https://www.r-project.org). LFB and qMRI values were averaged across the voxels within each ROI for each sample and were used as individual data points for the subsequent statistical analyses. A mixed-effect linear model with a qMRI parameter as the dependent variable was used; the independent variables include: sample ID modeled as a random effect to account for variability across the samples, tissue condition (fresh/thawed/fixed) modeled as a fixed effect, LFB (or qMRI parameter) modeled as a fixed effect explanatory variable for regression analysis, and an interaction term between the tissue condition and the explanatory variable when comparing two or more regression terms. A significant interaction term would indicate a difference between the slopes of the regression lines,

whereas a significant tissue condition term would indicate statistically different intercepts.

The plots were generated using mean-adjusted values derived from the mixed-effects models. The residuals after applying the random effect of sample ID were adjusted to the overall sample mean, which would account for the sample-to-sample variation, including the variability in staining and use of different coils. Unpaired t-tests with a Bonferroni corrected p-value threshold of 0.00625 were used for post-hoc pair-wise comparison between the tissue conditions to determine whether the thawed or fixed tissues significantly differed from the fresh samples. Correlation analysis was conducted across ROIs across all samples and separately for each sample.

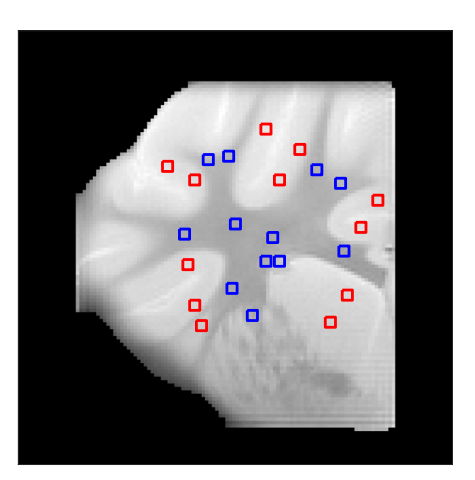
Power analysis: For a mixed-effect model, at least six samples per tissue preparation method and at least three ROIs per region (WM/GM) were needed to achieve a power of 90%, assuming an effect size of at least 10% of the control mean. These calculations were performed using the simr package (Version 1.07) function powerSim in R. We had 236 ROIs total (124 WM, 112 GM) across 14 samples (7 fixed, 7 thawed), with 5 to 24 ROIs per sample.

15222594, 2025, 5, Downloaded from https://onlinelibrary.wiley.com/doi/10.1002/mrm.30623 by University Of Michigan Library, Wiley Online Library on [28/08/2025]. See the Terms

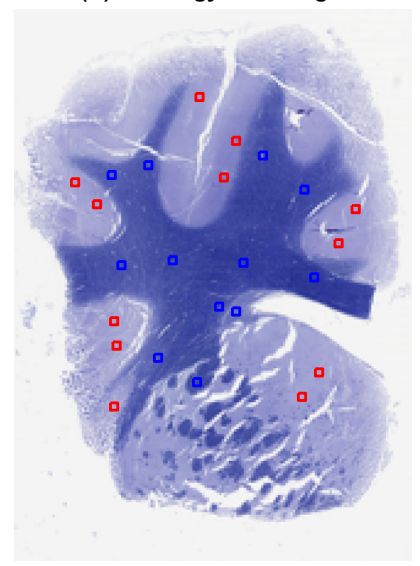
on Wiley Online Library for rules of use; OA articles are governed by the applicable Creative Commons

FIGURE 4 White matter (blue) and gray matter (red) ROIs labeled on a representative fresh sample spin echo image and the corresponding histology LFB image.

## (A) Spin Echo Image



#### (B) Histology LFB Image



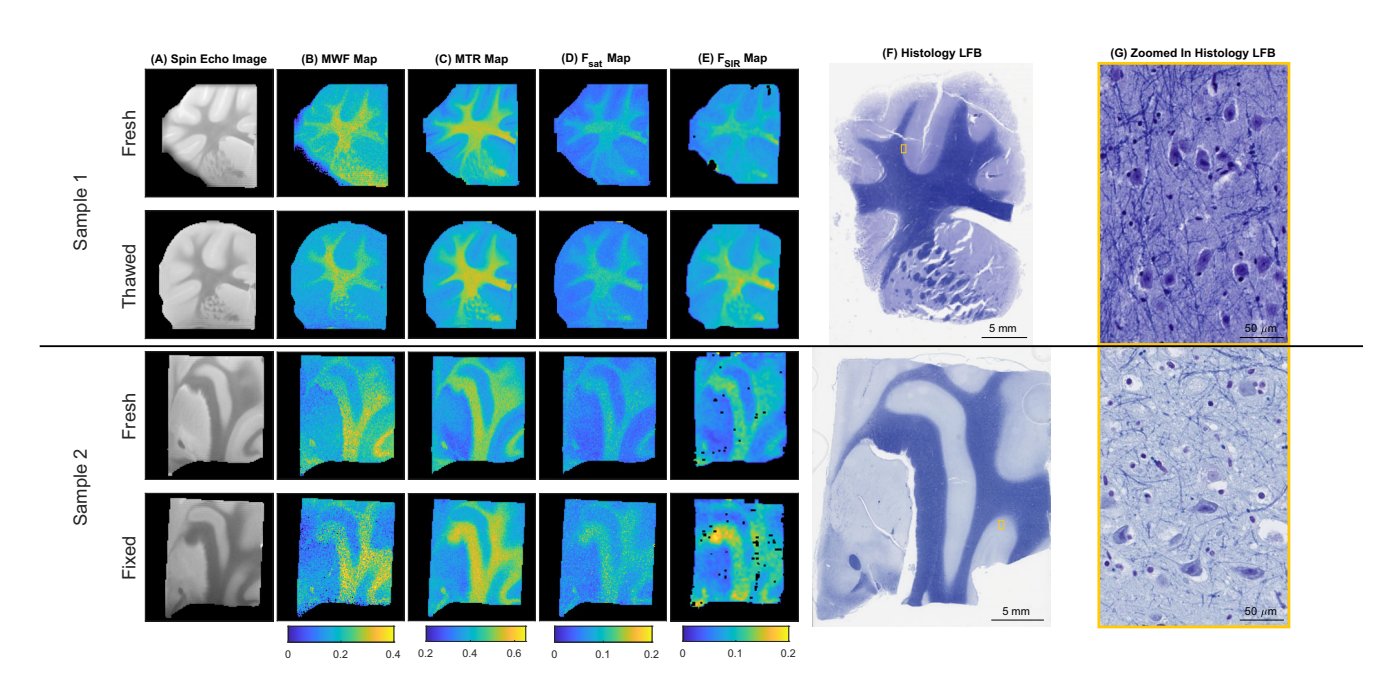


FIGURE 5 qMRI maps and histology stains for two representative sheep brain tissue samples. Sample 1 (rows 1–2, coronal slice) was scanned fresh and thawed, and Sample 2 (rows 3–4, sagittal slice) was scanned fresh and fixed. (A) Spin echo images at TE = 5 ms. (B) MWF maps calculated with a 20 ms cutoff; this value separated the peaks for most voxels, but black pixel outliers in maps are outlier voxels where the peaks were inconsistent with this cutoff. (C) MTR maps from MT contrast images at an average of -10 and 10 kHz off-resonance and 8.8  $\mu$ T power level. (D)  $F_{\text{sat}}$  maps. (E)  $F_{\text{SIR}}$  maps; black pixel outliers in maps are voxels where the fitting routine produced NaN values. (F) LFB histology for Samples 1–2. (G) Zoomed-in views showing cellular integrity.

#### 3 | RESULTS

Figure 5 shows qMRI parameter maps for two representative samples. Both samples were scanned fresh prior to tissue processing, followed by a second scan after a freeze-thaw cycle for Sample 1 and fixation for Sample 2. We observe similar contrasts in the maps across the different tissue conditions. As expected, a clear contrast was

maintained between the WM and GM structures. Visually, freezing or fixation did not significantly affect MR maps or WM/GM contrast. Figure 5 also includes the corresponding histology images; the zoomed-in images show myelinated axons as well as intact neurons, oligodendrocytes, and astrocytes for both tissue conditions. Freezing can cause morphological changes to the tissue, as demonstrated in the Sample 1 LFB image, where portions of the

FIGURE 6 Box plots (interquartile range, whiskers: 1.5-times interquartile range, outliers as dots) of average mean-adjusted MR parameters (across individual samples) from ROIs from all tissue samples. Parameter values are consistent with literature values. 5,10,26,45 For MTR and F<sub>sat</sub>, both thawed and fixed mean values were statistically different than fresh mean values for both WM and GM ROIs.

TABLE 1 Quantitative summary of fresh, thawed, and fixed mean qMRI parameter values in Figure 6.

ROIs			Mean $\pm$ standard deviation <i>P</i> -values				
Tissue condition	Туре	N	MWF	MTR	Fsat	FSIR	
Fresh	WM	102	$0.24 \pm 0.035$	$0.49 \pm 0.026$	$0.09 \pm 0.011$	$0.10 \pm 0.012$	
	GM	90	$0.16 \pm 0.026$	$0.38 \pm 0.022$	$0.056 \pm 0.0071$	$0.070 \pm 0.0096$	
Thawed	WM	51	$0.24 \pm 0.026$ p = 0.87	$0.52 \pm 0.027$ $p = 4.1 (10^{-10})$	$0.11 \pm 0.011$ $p = 1.4 (10^{-14})$	$0.12 \pm 0.016$ $p = 1.9 (10^{-13})$	
	GM	51	$0.17 \pm 0.020$ $p = 0.17$	$0.39 \pm 0.014$ $p = 0.0011$	$0.063 \pm 0.0053$ $p = 8.2 (10^{-10})$	$0.072 \pm 0.0076$ p = 0.030	
Fixed	WM	51	$0.24 \pm 0.054$ p = 0.91	$0.53 \pm 0.042$ $p = 4.2 (10^{-8})$	$0.10 \pm 0.014$ $p = 3.5 (10^{-6})$	$0.12 \pm 0.018$ $p = 9.5 (10^{-8})$	
	GM	39	$0.13 \pm 0.028$ $p = 3.2 (10^{-9})$	$0.39 \pm 0.025$ $p = 0.0026$	$0.074 \pm 0.014$ $p = 3.1 (10^{-11})$	$0.072 \pm 0.013$ $p = 0.16$	

Note: Mean ± standard deviation of qMRI parameter values for WM and GM ROI data for the three tissue conditions. Bold values in the thawed/fixed rows indicate statistically significant differences in the mean qMRI values between the thawed or fixed samples compared to the fresh samples from t-tests with a Bonferroni corrected threshold (p < 0.00625). P-values are from these t-tests. All qMRI parameter values are unitless fractions. N is the minimum number of ROIs pooled across all samples (some qMRI measures have data from more than N ROIs), as for some samples, not every qMRI measure was collected; see

sample have cracks. These cracks are also seen in fixed tissue, but based on visual inspection of the images, were more prevalent in samples that had been frozen.

Figure 6 pools average ROI data from all samples for the four qMRI parameters to show the effects of tissue preparation, separating data based on tissue condition and WM/GM data. The pooled data from the WM ROIs consistently showed a higher value than the GM ROIs, supporting the notion that these parameters are sensitive to myelin. Table 1 further quantifies the results in Figure 6 and includes the number of WM/GM ROIs and mean ± the standard deviation for each qMRI parameter for each tissue condition. The number of ROIs N represents the

minimum number of ROIs pooled across samples because some samples are missing data from one or more parameters; see Table S1 for more details. Overall, all thawed and fixed average measures were similar (within  $\pm 0.04$ ) to those of the fresh samples. T-tests detected statistically higher MTR and F<sub>sat</sub> in WM and GM and F<sub>SIR</sub> in WM in both thawed and fixed tissue compared to fresh. The results were comparable across tissue conditions for MWF, with the exception that GM MWF values were lower in fixed tissue compared to fresh, a finding that was not observed in the thawed samples.

Looking at average WM and GM values of qMRI parameters can mask the effects of tissue processing on the

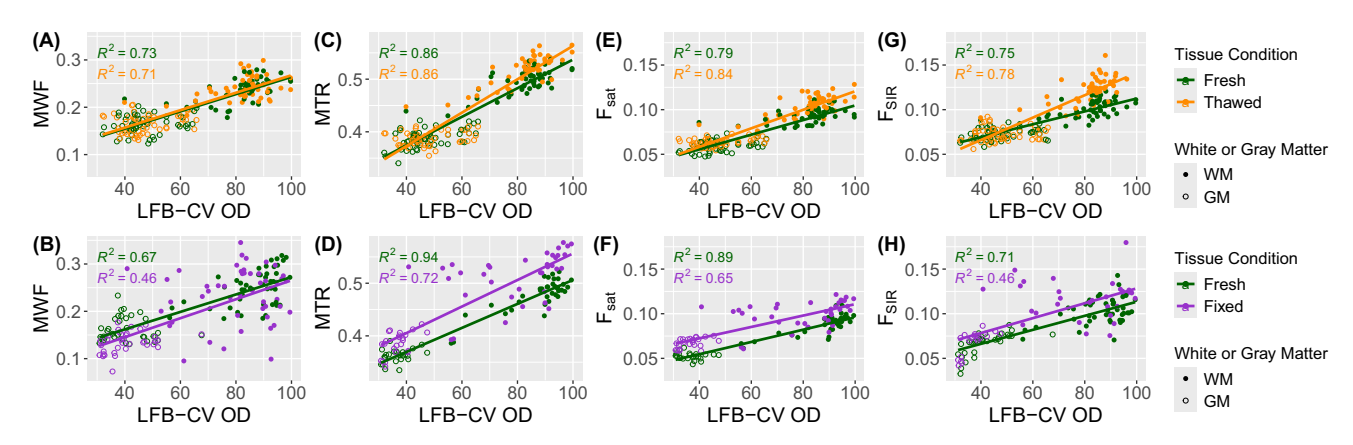


FIGURE 7 Correlation between qMRI parameter and histology luxol fast blue stain/cresyl violet counterstain (LFB-CV) mean-adjusted values across tissue samples for fresh and thawed (Row 1) and fresh and fixed (Row 2) samples. Fresh samples have been separated into two groups based on whether they went on to be frozen or fixed and were not pooled because each pair of scans for one sample corresponds to one LFB image. Fresh, thawed, and fixed qMRI parameters showed a strong correlation with LFB-CV OD for all ROIs as indicated by the high  $R^2$  values.

estimation of myelin content. Figure 6 exhibits some WM outlier data points with values more in line with GM; for example, some MWF WM points have a very low MWF. We chose ROIs that include a wide range of myelin content, as seen in Figure 4, so the WM-labeled ROIs included some structures with less myelin, such as the fornix and juxtacortical WM. Additionally, intermediate myelin content in WM structures may be affected differently by different tissue preparations. Figure 7 addresses these limitations of the box plots; it shows qMRI versus LFB values, which demonstrates their correlation and displays intermediate LFB values between the distinct WM and GM clusters. These LFB values include a counterstain; the contribution of the nuclear staining to the overall tissue staining was found to be minimal and relatively uniform given our scale and ROI size as seen in Figure S2. The graph pools ROI data from samples scanned fresh/thawed and samples scanned fresh/fixed separately; this was done because each pair of scans corresponds to the same LFB data. All qMRI parameters correlated with LFB, and for some plots the qMRI parameters correlated with LFB within the WM ROI subgroups. Table 2 includes quantitative metrics corresponding to Figure 7. It shows the correlation  $R^2$  values for each qMRI parameter for all ROIs pooled across all samples and for WM and GM ROIs separately in addition to the range of  $R^2$  values from correlation analysis conducted on each sample separately. The  $R^2$  values for all ROIs were high ( $\geq 0.45$ ) and statistically significant across tissue conditions, as were many of the WM-only and GM-only ROI  $R^2$  values, especially for MTR; this indicates that LFB accounts for a large variation in the MR signal. The MTR and F<sub>SIR</sub> fresh and thawed lines, and MWF fresh and fixed fitted lines had statistically different slopes, and

the MWF, MTR, and F<sub>sat</sub> fresh and fixed fitted lines had statistically different intercepts.

Figure 8 shows the correlation between each pair of qMRI parameters across ROIs for all tissue conditions. Unlike histology images, where image co-registration is difficult, qMRI-qMRI correlation analysis uses the same ROI coordinates across images. Using similar mixed-model analysis as with the LFB plots, in Figure 8C,E,F, the slopes and intercepts of the thawed sample data were significantly different from those of the fresh sample data were significantly different from the fresh, and in Figure 8A,D-F, the intercepts of the fixed sample data were significantly different from the fresh.

# 4 | DISCUSSION

Our findings suggest that alterations in qMRI parameters due to freezing and thawing tissue are comparable to those due to fixation. Although our results are overall consistent with prior studies, some notable differences are discussed below. Our ranges of MWF, MTR,  $F_{sat}$ , and  $F_{SIR}$  values are consistent with those of prior studies.  $^{4-7,26,43-45,61}$  The  $F_{sat}$  and  $F_{SIR}$  metrics had overall similar means, but the  $F_{SIR}$  means were  $\sim\!9\%$ –22% higher, except for the fixed GM case, where the  $F_{SIR}$  was 3% lower; further comparing these estimates is an investigation for future studies.

A few groups have studied the effects of tissue fixation on qMRI parameters. In a study of MWF and  $F_{sat}$  values in fresh and fixed 20 mm human spinal cord samples, <sup>10</sup> Seifert et al. reported an increase of around 40% in MWF for both WM and GM after 24 h of fixation in 10% formalin

TABLE 2 Quantitative summary of qMRI–LFB correlation in Figure 7.

ROIs			MWF	MTR	Fsat	FSIR
Tissue condition	Туре	N	Overall R <sup>2</sup> (range)	Overall R <sup>2</sup> (range)	Overall R <sup>2</sup> (range)	Overall R <sup>2</sup> (range)
Fresh	WM	51	0.31	0.51	0.26	0.20
	GM	51	_	0.24	0.11	_
	All	102	0.73 (0.75–0.93)	0.86 (0.83–0.98)	0.79 (0.70–0.95)	0.75 (0.63–0.91)
Thawed	WM	51	0.16	0.67	0.48	0.46
	GM	51	_	_	0.14	_
	All	102	0.70 (0.64–0.95)	0.86 (0.74–0.98)	0.84 (0.80-0.94)	0.79 (0.70–0.96)
Fresh/thawed interaction	All	102	_	s(p = 0.022)	s(p = 0.028)	_
Fresh	WM	36	0.25	0.69	0.59	0.13
	GM	24	_	_	_	0.44
	All	60	0.66 (0.62–0.88)	0.94 (0.93–0.96)	0.89 (0.86–0.94)	0.75 (0.76–0.78)
Fixed	WM	36	_	0.15	0.11	_
	GM	24	0.097	0.29	0.19	0.48
	All	60	0.45 (0.42–0.86)	0.71 (0.52–0.98)	0.64 (0.46–0.92)	0.45 (0.32–0.93)
Fresh/fixed interaction	All	60	s (p = 0.034) i $(p = 0.0076)$	i(p = 0.034)	$i(p = 8.3(10^{-6}))$	_

Note:  $R^2$  values for correlation between qMRI measures and LFB across WM ROIs only, GM ROIs only, and all ROIs (WM and GM). Values are shown as  $R^2$  for mean—adjusted data pooled across all samples. Ranges of  $R^2$  values for individual samples are shown in parenthesis for the "All" rows. With one exception (fresh MWF correlation), the overall  $R^2$  values are within the range of the individual sample  $R^2$  values. Dash marks represent  $R^2$  values that were not statistically significant (p < 0.05). This table corresponds to the data in Figure 7. Yellow rows show results and corresponding p-values from the interaction term between tissue condition and LFB from the mixed- effect model analysis ("s:" statistically different slopes, "i:" statistically different intercepts); statistical significance indicates differential correlation based on tissue condition. N is the minimum number of ROIs pooled across all samples (some qMRI measures have data from more than N ROIs), as for some samples, not every measure (qMRI or LFB) was collected; see Table S1.

compared to the pre-fixation measurement, 10 which was similar to the observations by Chen et al.<sup>23</sup> Our results, however, show that WM MWF values were not significantly affected by 36 h of fixation in formalin, and GM values actually decreased by about 19%. Our study design differs from that of Seifert et al. in many aspects, as our studies involved different anatomical sites, and we used sheep brain tissue, whereas Seifert et al. used human spinal cord tissue. Our study was conducted at a lower temperature, and MWF has been shown to depend on temperature. 62 In addition, we submerged formalin-fixed tissue in buffered saline solution for 12 h prior to scanning, whereas Seifert et al. washed the tissue for multiple 24-hour periods, which could have altered the tissue water content. Since WM and GM may have different susceptibilities to water fluctuations, differences in the duration of

the saline wash could have affected GM MWF values more than WM.

Our MT related measures are consistent with previous studies. We saw a statistically significant increase in MTR and  $F_{sat}$  after fixation, although to a lesser degree than previously reported. For  $F_{sat}$ , Seifert et al. found approximately a 37% increase in WM and a 12% increase in GM after one day of fixation. We found an approximate 11% increase in WM and 32% increase in GM after 36 h of fixation. For MTR, we found an 8% increase in WM and 3% increase in GM, and for  $F_{SIR}$  a 20% increase in WM and 3% increase in GM. The overall smaller change in MT measures due to fixation in our studies could be due to similar factors as for MWF, or the choice of ROIs could contribute to some of the observed differences. We selected ROIs to include less myelinated regions of WM, such as the

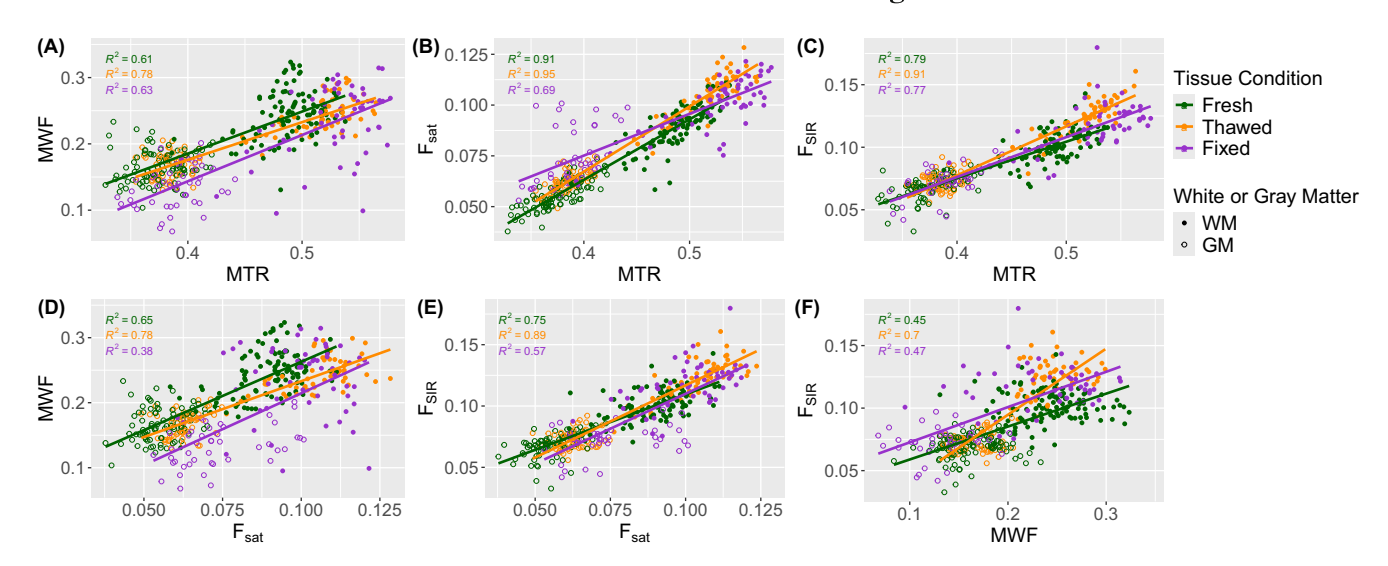


FIGURE 8 Correlation among each pair of qMRI parameter mean-adjusted values across tissue samples for fresh, thawed, and fixed samples. Fits are similar among tissue conditions for all pairs of parameters, further suggesting that thawed samples are a viable option for qMRI analysis. MTR and  $F_{sat}$  correlate well, likely because both are calculated from the off-resonance RF saturation MT scans.  $F_{SIR}$  also correlates well with MTR and  $F_{sat}$ , which may result from it also being an MT parameter.

fornix and juxtacortical myelin, which may have affected the mean qMRI values. Our sequences and fitting methods also differed from Seifert et al., which may have affected the results.

A potential explanation for the observed changes in the qMT parameters after tissue fixation is that the fixation expands the spaces between layers of the myelin sheath, which may increase exchange between the macromolecular proton and water pools and increase  $F_{sat}$ . Formalin cross-links protein lysine residues, which may increase semi-solid content, creating more pathways for MT and increasing MTR.

We also saw significant increases in thawed tissue MTR and  $F_{sat}$  in both WM (6% and 22%) and GM (3% and 13%) and in the  $F_{SIR}$  in WM (20%) on the same order of the increases from fixation. Evans et al.<sup>24</sup> also found that freezing muscle tissue increases MTR, which is consistent with our results, but given the different tissue types, any comparison must be viewed cautiously. Whether the increases in MTR,  $F_{sat}$ , and  $F_{SIR}$  in frozen tissue are due to similar mechanisms as the effect of fixation requires additional studies with closer inspection of morphological changes with electron microscopy.

Examining the relationship between qMRI and non-MR measures of myelin content across a wide range of myelin concentration affords additional insight into the effects of tissue preparation on qMRI measures as they relate to other measures such as LFB. Overall, all qMRI parameters correlated well with LFB as in previous studies, 4-6,8,9 even when pooling ROIs from different samples and in WM ROIs alone. 62,63 As mentioned in

Section 3, the slopes of the qMRI versus LFB plots are generally higher in thawed samples as compared to fresh, indicating that the freeze-thaw cycle increases the gMRI signal more for the WM than GM ROIs. This trend reached statistical significance only for MTR and F<sub>sat</sub>. In the case of the fixed tissue, the intercepts of the fitted lines were affected for MWF, MTR, and Fsat. Tissue fixation appears to affect the WM to the same extent that it affects the GM, thereby increasing the intercepts of qMRI measures of myelin content without as strongly affecting the slopes. We saw a similar trend in the qMRI versus qMRI plots, confirming that the observed trends hold without potential errors due to registration mismatch. The strong correlation in these plots was consistent with prior reports. 10,63 We also observe a similar trend with MTsat, another qMRI parameter sensitive to myelin content. 64-70 Although this parameter has been excluded from the main text, we include MTsat maps and histological correlation analysis in Figures S4 and S5.

The correlation analysis results indicate that freezing and fixation may affect qMRI tissue parameters differently; freezing could potentially alter the WM structures that contain thicker and more abundant myelin sheaths more robustly than thinner myelinated axons in the GM, whereas fixation could potentially affect the myelination in WM and GM uniformly. We hypothesize that formalin fixation, being a chemical process, may be less dependent on the morphological features of the tissue such as fiber diameter and the number of myelin layers, which may affect WM and GM equally. In contrast, freezing and thawing are thermo-mechanical processes that we conjecture

may be affected by the microscopic morphology of the tissue and fiber diameter, thereby having a differential effect on WM and GM. MWF and MTR have been shown to depend on WM fiber orientation and thickness, 63,71 but further studies are needed to elucidate the mechanisms behind our observations and to test these hypotheses.

Our study unveils many challenges and limitations in evaluating the effects of post-mortem tissue preparation on qMRI measures, including use of different coils for scanning, lack of strict temperature control, use of semi-quantitative measures of myelin (LFB-CV), variability in the time of death to scan across the samples, lack of stereotactic dissection of tissue and image registration, among others. We attempted to mitigate or account for some of these shortcomings as discussed below. Because we obtained our samples from a vendor, the post-mortem interval ranged from 12 to 13 days; however, care was taken to refrigerate or keep on ice to minimize tissue autolysis, and our histological examination confirmed tissue preservation throughout the process, as seen in Figure 5. A slight difference in postmortem interval may have affected qMRI results due to increased exchange from breakdown of the cellular membranes.

Additionally, freezing, thawing, and fixation deform the tissue and cause shrinkage and/or expansion, which makes histology-MR image registration challenging, leading us to choose to use manual matching for ROI analysis instead of registration. We selected regions that had clear anatomical demarcation to minimize the effects of slice selections between MR and histology images, but errors in ROI placement undoubtedly remain. These variations may lead to outliers in the data; for example, impacting why the fixed GM MWF values were lower than their fresh counterparts and why the MWF plots had lower  $R^2$  values in Figure 7. Figure 8 is immune to these ROI placement errors; however, imperfect unwarping of the EPI data and registration to the MESE data could also have led to outliers in the  $F_{\rm SIR}$  values and lower  $R^2$  values.

Our data indicate that the cells remained intact during the freezing/thawing process of around two weeks; however, the long-term effects of tissue freezing remain unknown. Further experiments such as those in Seifert et al.  $^{10}$  are needed to determine how freezing and fixation time affect each of the estimated parameters. Scanning tissue at lower temperature ( $\sim$ 15°C–20°C) has the advantage of preserving tissue for longer, which is especially important when working with unfixed specimens; however, in a separate experiment (not shown) we conducted IR scans of a fixed sample at 19.8°C and 16.3°C and found the  $F_{SIR}$  value to be  $\sim$ 10%–20% higher at the lower temperature. Further experiments are needed to evaluate the effect of temperature on qMRI parameters for different tissue conditions. We did not monitor the temperature as the samples

equilibrated from room temperature to the cooler ambient temperature of the magnet at  $\sim 15^{\circ}\text{C}$ . Therefore, we cannot report the exact temperature, which is a limitation of our study.

Multi-slice MESE acquisitions are affected by MT.  $^{51,72}$  In a separate experiment (not shown), we compared parameter estimates from single and multi-slice MESE and IR acquisitions in a fixed sample. On average, the MWF/F<sub>SIR</sub> values estimated from the multi-slice acquisitions increased/decreased from the single-slice acquisition by 10%-20%; thus, our use of multi-slice acquisitions is a limitation of our work. To estimate qMT parameters with the off-resonance RF saturation model we fixed  $R_{1,\rm f}$  to  $0.33~{\rm s}^{-146}$  rather than estimating it using the IR data  $^{30,31}$  as this resulted in better qMT parameter fits. Fixing  $R_{1,\rm f}$  likely underestimated  $F_{\rm sat}$ , made the  $F_{\rm sat}$  values more sensitive to  $T_1$ , and affected our WM/GM comparisons due to WM/GM differences in  $T_1$ ; thus this is a limitation of this study.

Future studies could also examine the effects of freezing and fixation on MTsat further and on inhomogeneous magnetization transfer (ihMT) imaging, as the ihMT ratio (ihMTR) has been shown to be more specific to myelin than MTR.<sup>62,63,73</sup> Other modalities such as ultrashort TE (UTE) imaging, quantitative susceptibility mapping (QSM), and quantitative diffusion methods could also be explored.

#### 5 | CONCLUSION

Thawed and fixed tissue MR parameter values differed modestly compared to fresh values. Both tissue preparations had similar effects on myelin-sensitive qMRI parameter values, and the samples maintained cell integrity, allowing histology to be conducted. Thus, tissue freezing is a reasonable alternative tissue preservation method to fixation for use in qMRI analysis. However, it is important to take into consideration that various tissue preparation techniques may differentially affect regions with varying myelin content or morphology.

#### **ACKNOWLEDGMENTS**

We thank Steven T. Whitaker for sharing his Julia MESE analysis code and the researchers at the University of British Columbia MRI Research Centre for their helpful discussions. We also thank the reviewers for their comments, which greatly improved the paper.

## **CONFLICT OF INTEREST STATEMENT**

The authors declare no potential conflicts of interest.

#### DATA AVAILABILITY STATEMENT

Data from the 14 samples are available here:<sup>74</sup> https://doi.org/10.7302/dp7t-c323.

#### ORCID

Amaya Murguia https://orcid.org/0009-0004-5546

Scott D. Swanson https://orcid.org/0000-0002-4714-4031

Ulrich Scheven https://orcid.org/0000-0001-8111-0081

Andrea Jacobson https://orcid.org/0009-0001-4507

-8464

Jeffrey A. Fessler https://orcid.org/0000-0001-9998-3315 Navid Seraji-Bozorgzad https://orcid.org/0000-0002 -8215-6513

#### REFERENCES

- Piredda GF, Hilbert T, Thiran J-P, Kober T. Probing myelin content of the human brain with MRI: A review. Magn Reson Med. 2021;85:627-652.
- 2. Mackay A, Whittall K, Adler J, Li D, Paty D, Graeb D. In vivo visualization of myelin water in brain by magnetic resonance. *Magn Reson Med*. 1994;31:673-677.
- Papuć E, Rejdak K. The role of myelin damage in Alzheimer's disease pathology. *Rchives Med Sci.* 2018;16:341-345.
- Laule C, Leung E, Li DKB, et al. Myelin water imaging in multiple sclerosis: quantitative correlations with histopathology. *Mult Scler J*. 2006;12:747-753.
- Laule C, Kozlowski P, Leung E, Li DKB, MacKay AL, Moore GRW. Myelin water imaging of multiple sclerosis at 7 T: correlations with histopathology. *NeuroImage*. 2008;40: 1575-1580.
- Laule C, Vavasour IM, Leung E, et al. Pathological basis of diffusely abnormal white matter: insights from magnetic resonance imaging and histology. *Mult Scler*. 2011;17: 144-150
- 7. Laule C, Moore GRW. Myelin water imaging to detect demyelination and remyelination and its validation in pathology. *Brain Pathol.* 2018;28:750-764.
- 8. Deloire-Grassin MSA, Brochet B, Quesson B, et al. In vivo evaluation of remyelination in rat brain by magnetization transfer imaging. *J Neurol Sci.* 2000;178:10-16.
- 9. Schmierer K, Tozer DJ, Scaravilli F, et al. Quantitative magnetization transfer imaging in postmortem multiple sclerosis brain. *J Magn Reson Imaging*. 2007;26:41-51.
- Seifert Alan C, Melissa U, Marco H, Mary F, Junqian X. Formalin tissue fixation biases myelin-sensitive MRI. Magn Reson Med. 2019;82:1504-1517.
- 11. Puchtler H, Meloan SN. On the chemistry of formaldehyde fixation and its effects on immunohistochemical reactions. *Histochemistry*. 1985;82:201-204.
- 12. Shabihkhani M, Lucey GM, Wei B, et al. The procurement, storage, and quality assurance of frozen blood and tissue biospecimens in pathology, biorepository, and biobank settings. *Clin Biochem.* 2014;47:258-266.

- Rosene DL, Rhodes KJ. Cryoprotection and freezing methods to control ice crystal artifact in frozen sections of fixed and unfixed brain tissue. *Methods in Neurosciences*. Vol 3; 1990:360-385. Academic Press.
- Whittall KP, MacKay AL. Quantitative interpretation of NMR relaxation data. J Magn Reson. 1969;84:134-152.
- MacKay A, Laule C, Vavasour I, Bjarnason T, Kolind S, Mädler B. Insights into brain microstructure from the T2 distribution. Magn Reson Imaging. 2006;24:515-525.
- Shatil Anwar S, Nasir UM, Matsuda Kant M, Figley CR. Quantitative ex vivo MRI changes due to progressive formalin fixation in whole human brain specimens: longitudinal characterization of diffusion, relaxometry, and myelin water fraction measurements at 3T. Front Med. 2018;5:31.
- 17. Chen HS-M, Holmes N, Liu J, Tetzlaff W, Kozlowski P. Validating myelin water imaging with transmission electron microscopy in a rat spinal cord injury model. *NeuroImage*. 2017;153:122-130.
- Dawe RJ, Bennett DA, Schneider JA, Vasireddi SK, Arfanakis K. Postmortem MRI of human brain hemispheres: T2 relaxation times during formaldehyde fixation. *Magn Reson Med.* 2009:61:810-818.
- Raman MR, Shu Y, Lesnick TG, Jack CR, Kantarci K. Regional T1 relaxation time constants in ex vivo human brain: longitudinal effects of formalin exposure. *Magn Reson Med*. 2017;77:774-778.
- Blamire AM, Rowe JG, Styles P, McDonald B. Optimising imaging parameters for post mortem MR imaging of the human brain. *Acta Radiol.* 1999;40:593-597.
- Carvlin MJ, Asato R, Hackney DB, Kassab E, Joseph PM. High-resolution MR of the spinal cord in humans and rats. Am J Neuroradiol. 1989;10:13-17.
- Fishbein Kenneth W, Gluzband Yehezkiel A, Masaru K, et al. Effects of formalin fixation and collagen cross-linking on T2 and magnetization transfer in bovine nasal cartilage. *Magn Reson Med*. 2007;57:1000-1011.
- Chen HS-M, Liu J, MacKay AL, Tetzlaff W, Kozlowski P. Effect of aldehyde fixation on the myelin water fraction measurement in rat cervical spinal cord. *Proc Int Soc Magn Reson Med*. 2018:852.
- Evans Stephen D, Nott Kevin P, Kshirsagar Ashwini A, Hall LD.
   The effect of freezing and thawing on the magnetic resonance imaging parameters of water in beef, lamb and pork meat. *Int J Food Sci Technol.* 1998;33:317-328.
- 25. Baadsvik EL, Weiger M, Froidevaux R, Faigle W, Ineichen BV, Pruessmann KP. Mapping the myelin bilayer with short-T2 MRI: methods validation and reference data for healthy human brain. *Magn Reson Med.* 2023;89:665-677.
- 26. Stanisz GJ, Odrobina EE, Pun J, et al. T1, T2 relaxation and magnetization transfer in tissue at 3T. *Magn Reson Med.* 2005;54:507-512.
- Stanisz GJ, Kecojevic A, Bronskill MJ, Henkelman RM. Characterizing white matter with magnetization transfer and T2. Magn Reson Med. 1999;42:1128-1136.
- Kucharczyk W, Macdonald PM, Stanisz GJ, Henkelman RM. Relaxivity and magnetization transfer of white matter lipids at MR imaging: importance of cerebrosides and pH. *Radiology*. 1994;192:521-529.
- Grossman RI. Magnetization transfer in multiple sclerosis. Ann Neurolog. 1994;36:S97-S99.

- 30. Henkelman RM, Huang X, Xiang Q-S, Stanisz GJ, Swanson SD, Bronskill MJ. Quantitative interpretation of magnetization transfer. *Magn Reson Med.* 1993;29:759-766.
- 31. Sled JG, Pike GB. Quantitative imaging of magnetization transfer exchange and relaxation properties in vivo using MRI. *Magn Reson Med*. 2001;46:923-931.
- 32. Janve Vaibhav A, Zhongliang Z, Song-Yi Y, et al. The radial diffusivity and magnetization transfer pool size ratio are sensitive markers for demyelination in a rat model of type III multiple sclerosis (MS) lesions. *NeuroImage*. 2013;74:298-305.
- Turati L, Moscatelli M, Mastropietro A, et al. In vivo quantitative magnetization transfer imaging correlates with histology during de-and remyelination in cuprizone-treated mice. NMR Biomed. 2015;28:327-337.
- Odrobina Ewa E, Lam Toby YJ, Teresa P, Rajiv M, Stanisz GJ. MR properties of excised neural tissue following experimentally induced demyelination. NMR Biomed. 2005;18:277-284.
- 35. Schmierer K, Wheeler-Kingshott CAM, Tozer DJ, et al. Quantitative magnetic resonance of postmortem multiple sclerosis brain before and after fixation. *Magn Reson Med*. 2008;59:268-277.
- Schmierer K, Thavarajah Janet R, An Shu F, Brandner S, Miller David H, Tozer DJ. Effects of formalin fixation on magnetic resonance indices in multiple sclerosis cortical gray matter. *J Magn Reson Imaging*. 2010;32:1054-1060.
- Rioux JA, Levesque Ives R, Rutt BK. Biexponential longitudinal relaxation in white matter: characterization and impact on T1 mapping with IR-FSE and MP2RAGE. *Magn Reson Med*. 2016;75:2265-2277.
- 38. Stüber C, Morawski M, Schäfer A, et al. Myelin and iron concentration in the human brain: a quantitative study of MRI contrast. *NeuroImage*. 2014;93:95-106.
- Shams Z, Norris DG, Marques JP. A comparison of in vivo MRI based cortical myelin mapping using T1w/T2w and R1 mapping at 3T. PLoS One. 2019;14:e0218089.
- 40. Labadie C, Lee J-H, Rooney William D, et al. Myelin water mapping by spatially regularized longitudinal relaxographic imaging at high magnetic fields. *Magn Reson Med.* 2014;71:375-387.
- 41. Gochberg Daniel F, Gore JC. Quantitative imaging of magnetization transfer using an inversion recovery sequence. *Mag Reson Med*. 2003;49:501-505.
- 42. Gochberg DF, Kennan RP, Robson MD, Gore JC. Quantitative imaging of magnetization transfer using multiple selective pulses. *Magn Reson Med.* 1999;41:1065-1072.
- 43. Gochberg DF, Gore JC. Quantitative magnetization transfer imaging via selective inversion recovery with short repetition times. *Magn Reson Med*. 2007;57:437-441.
- 44. Li K, Zu Z, Xu J, et al. Optimized inversion recovery sequences for quantitative T1 and magnetization transfer imaging. *Magn Reson Med*. 2010;64:491-500.
- 45. Dortch RD, Li KE, Gochberg DF, et al. Quantitative magnetization transfer imaging in human brain at 3 T via selective inversion recovery. *Magn Reson Med*. 2011;66:1346-1352.
- Wang Y, Gelderen P, Zwart Jacco A, Duyn JH. B0-field dependence of MRI T1 relaxation in human brain. *NeuroImage*. 2020;213:116700.
- 47. Assländer J, Mao A, Marchetto E, et al. Unconstrained quantitative magnetization transfer imaging: disentangling T1 of the free and semi-solid spin pools. *Imaging Neurosci.* 2024;2:1-16.

- 48. Murguia A, Swanson Scott D, Scheven U, Nielsen J-F, Fessler Jeffrey A, Navid S-B. Characterizing Tissue Relaxation and Magnetization Transfer in Fresh, Thawed, and Fixed White Matter Tissue Samples. Proceedings of the 32nd Annual Meeting of the International Society for Magnetic Resonance in Medicine, Singapore; 2024:2036.
- 49. Murguia A, Jacobson A, Swanson Scott D, et al. Impact of Tissue Sample Preparation Method on Myelin-Sensitive Quantitative MR Imaging and Histological Analysis. *Proceedings of the 33rd Annual Meeting of the International Society for Magnetic Resonance in Medicine*; 2025:1484.
- Wiggermann V, Vavasour IM, Kolind SH, MacKay Alexander L, Helms G, Rauscher A. Non-negative least squares computation for in vivo myelin mapping using simulated multi-echo spin-echo T2 decay data. NMR Biomed. 2020;33:e4277.
- Prasloski T, Mädler B, Xiang Q-S, MacKay A, Jones C. Applications of stimulated echo correction to multicomponent T2 analysis. Magn Reson Med. 2012;67:1803-1814.
- Swanson SD. Transient and Steady-State Effects of Indirect RF Saturation in Heterogeneous Systems. Proceedings of the 11th Annual Meeting of the International Society for Magnetic Resonance in Medicine: 1992:255.
- Wennerström H. Proton nuclear magnetic resonance lineshapes in lamellar liquid crystals. Chem Phys Lett. 1973;18:41-44.
- 54. Morrison C, Stanisz G, Henkelman RM. Modeling magnetization transfer for biological-like systems using a semi-solid pool with a super-Lorentzian lineshape and dipolar reservoir. *J Magn Reson B.* 1995;108:103-113.
- 55. Morrison C, Mark HR. A model for magnetization transfer in tissues. *Magn Reson Med*. 1995;33:475-482.
- 56. Helms G, Hagberg GE. In vivo quantification of the bound pool T1 in human white matter using the binary spin-bath model of progressive magnetization transfer saturation. *Phys Med Biol.* 2009;54:N529.
- 57. Silver Michael S, Joseph Richard I, Hoult DI. Highly selective  $\pi 2$  and  $\pi$  pulse generation. *J Magn Reson.* 1969;59:347-351.
- Jezzard P, Balaban RS. Correction for geometric distortion in echo planar images from B0 field variations. *Magn Reson Med*. 1995;34:65-73.
- 59. Dortch RD, Moore J, Li KE, et al. Quantitative magnetization transfer imaging of human brain at 7 T. *NeuroImage*. 2013;64:640-649.
- 60. Cercignani M, Bouyagoub S. Brain microstructure by multi-modal MRI: Is the whole greater than the sum of its parts? *NeuroImage*. 2018;182:117-127.
- 61. Smith AK, Lyttle Bailey D, Dortch RD, et al. Evaluating single-point quantitative magnetization transfer in the cervical spinal cord: application to multiple sclerosis. *NeuroImage: Clinical*. 2017;16:58-65.
- 62. Prevost Valentin H, Andrew Y, Morris Sarah R, et al. Temperature dependence and histological correlation of inhomogeneous magnetization transfer and myelin water imaging in ex vivo brain. *NeuroImage*. 2021;236:118046.
- 63. Morris SR, Vavasour IM, Smolina A, et al. Myelin biomarkers in the healthy adult brain: Correlation, reproducibility, and the effect of fiber orientation. *Magn Reson Med.* 2023;89: 1809-1824.
- 64. Helms G, Dathe H, Kallenberg K, Dechent P. High-resolution maps of magnetization transfer with inherent correction for

15222594, 2025, 5, Downloaded from https://onlinelibrary.wiley.com/doi/10.1002/mrm.30623 by University Of Michigan Library, Wiley Online Library on [28/08/2025]. See the Terms and Conditions (https://onlinelibrary.wiley.

ions) on Wiley Online Library for rules of use; OA articles are governed by the applicable Creative Commons

- RF inhomogeneity and T1 relaxation obtained from 3D FLASH MRI. Magn Reson Med. 2008;60:1396-1407.
- 65. Rahman N, Ramnarine J, Xu K, Brown A, Baron CA. Test-Retest Reproducibility of In Vivo Magnetization Transfer Ratio and Saturation Index in Mice at 9.4 Tesla. J Magn Reson Imaging. 2022;56:893-903.
- 66. Hagiwara A, Hori M, Kamagata K, et al. Myelin measurement: comparison between simultaneous tissue relaxometry, magnetization transfer saturation index, and T1w/T2w ratio methods. Sci Rep. 2018;8:10554.
- 67. Lema A, Bishop C, Malik O, et al. A comparison of magnetization transfer methods to assess brain and cervical cord microstructure in multiple sclerosis. J Neuroimaging. 2017;27:221-226.
- 68. Pike GB. Pulsed magnetization transfer contrast in gradient echo imaging: a two-pool analytic description of signal response. Magn Reson Med. 1996;36:95-103.
- 69. Olsson H, Andersen M, Wirestam R, Helms G. Mapping magnetization transfer saturation (MTsat) in human brain at 7T: Protocol optimization under specific absorption rate constraints. Magn Reson Med. 2021;86:2562-2576.
- 70. Krishnan S, Cler Gabriel J, Smith Harriet J, et al. Quantitative MRI reveals differences in striatal myelin in children with DLD. elife. 2022;11:e74242.
- 71. Harkins Kevin D, Dula Adrienne N, Does MD. Effect of intercompartmental water exchange on the apparent myelin water fraction in multiexponential T2 measurements of rat spinal cord. Magn Reson Med. 2012;67:793-800.
- 72. Vavasour IM, Whittall KP, Li DKB, MacKay AL. Different magnetization transfer effects exhibited by the short and long T2 components in human brain. Magn Reson Med. 2000;44:860-866.
- 73. Swanson SD, Malyarenko DI, Fabiilli ML, Welsh RC, Nielsen J-F, Srinivasan A. Molecular, dynamic, and structural origin of inhomogeneous magnetization transfer in lipid membranes. Magn Reson Med. 2017;77:1318-1328.
- 74. Murguia A, Swanson SD, Scheven U, et al.. (2025). Data for "Impact of Tissue Sample Preparation Methods on Myelin-Sensitive Quantitative MR Imaging" [Data set]. University of Michigan - Deep Blue Data. doi: 10.7302/dp7t-c323

#### SUPPORTING INFORMATION

Additional supporting information may be found in the online version of the article at the publisher's website.

**Data S1.** Supporting Information.

Figure S1. Illustration of the sheep brain dissection and sample selection. The sheep brains were cut into approximately 13 mm coronal sections. The 3rd most rostral section, which was at the level of caudate nucleus, was selected for MR and histological analysis.

**Figure S2**. LFB + Cresyl Violet plotted against LFB only values (blue minus red channel) across WM ROIs (2 mm diameter circles) show a strong correlation between the two measures and a slope of nearly 1 from linear regression

analysis. As expected, the intercept has a positive value (14), indicating a small residual stain for the nuclei in the absence of myelin staining. The plot shows that using a counterstain has little effect on the estimate of myelin content as compared to LFB alone, at least in ROIs on the order

Figure S3. Comparison of hyperbolic secant and Gaussian inversion pulses. (a) IR images (TI = 10 ms) for data collected with the the hyperbolic secant (HS) adiabatic full passage (AFP) inversion pulse<sup>57</sup> and Gaussian inversion pulse. (b) Observed and fitted signal recovery curves vs. inversion time for one WM voxel and one GM voxel in the ROI. (c) Map of the estimated long T1 value for each voxel. (d) Normalized corresponding signal amplitude for the long  $T_1$  component (as<sub>low</sub>) for each voxel. (e) Map of the estimated short T<sub>1</sub> value for each voxel. (f) Normalized corresponding signal amplitude for the short T1 component (af<sub>ast</sub>) for each voxel. (g) F<sub>SIR</sub> map.

Figure S4. MTR and MTsat maps for two representative samples including the fresh/thawed and fresh/fixed versions of each sample. (a) MTR maps from MT contrast images at average of -10 and 10 kHz off-resonance and 8.8 µT for fresh/thawed sample. (b) MTR maps for fresh/ fixed sample. (c) MTsat maps generated as described above for fresh/thawed sample. (d) MTsat maps for fresh/fixed sample.

Figure S5. Correlation between MTR and MTsat parameters and histology LFB-CV mean-adjusted values across tissue samples for fresh and thawed (Row 1) and fresh and fixed (Row 2) samples. Both MTR and MTsat a show strong correlation with LFB-CV OD for all ROIs as indicated by the high  $R^2$  values. MTsat exhibits a similar trend to the plots in Figure 7 in the main text based on the mixed-model analysis described in the methods section 2.5. (a,b) exhibit a statistically significant (p < 0.05) difference in slopes between the fresh/thawed fits (a: p = 0.022, b: p = 0.0039) and (c,d) exhibit a statistically significant (p < 0.05) difference in intercepts between the fresh/fixed fits (c: p = 0.033, d: p = 0.028).

How to cite this article: Murguia A, Swanson SD, Scheven U, et al. Impact of tissue sample preparation methods on myelin-sensitive quantitative MR imaging. Magn Reson Med. 2025;94:2071-2085. doi: 10.1002/mrm.30623

# Impact of Tissue Sample Preparation Methods on Myelin-Sensitive Quantitative MR Imaging

Amaya Murguia, Scott D. Swanson, Ulrich Scheven, Andrea Jacobson, Jon-Fredrik Nielsen, Jeffrey A. Fessler, Navid Seraji-Bozorgzad University of Michigan

# **Supporting Information**

# S1 | EXTRA SAMPLE INFORMATION

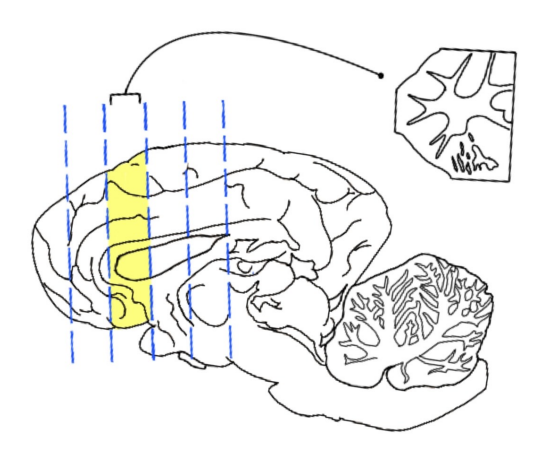


**FIGURE S1** Illustration of the sheep brain dissection and sample selection. The sheep brains were cut into approximately 13 mm coronal sections. The 3rd most rostral section, which was at the level of caudate nucleus, was selected for MR and histological analysis.

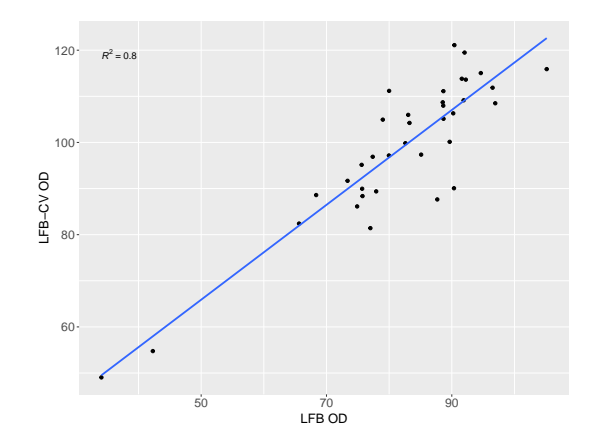


**FIGURE S2** LFB + Cresyl Violet plotted against LFB only values (blue minus red channel) across WM ROIs (2 mm diameter circles) show a strong correlation between the two measures and a slope of nearly 1 from linear regression analysis. As expected, the intercept has a positive value (14), indicating a small residual stain for the nuclei in the absence of myelin staining. The plot shows that using a counterstain has little effect on the estimate of myelin content as compared to LFB alone, at least in ROIs on the order of 2 mm.

TABLE S1 Quantitative MRI Parameters and Histology Data Tally for All Samples

Samples		Parameter						
ID	Tissue Condition	MWF	MTR	$F_{sat}$	$F_{SIR}$	LFB-CV		
S1	Fresh	<b>✓</b>	<b>✓</b>	<b>✓</b>	<b>✓</b>	<b>✓</b>		
	Thawed	<b>✓</b>	<b>~</b>	<b>✓</b>	<b>✓</b>	<b>✓</b>		
S2	Fresh	✓ ✓	<b>✓</b>	<b>✓</b>	<b>✓</b>	<b>✓</b>		
	Thawed	<b>✓</b>	<b>✓</b>	<b>/</b>	<b>✓</b>	<b>✓</b>		
	Fresh	<b>✓</b>	<b>✓</b>	<b>/</b>	<b>/</b>	<b>✓</b>		
<b>S3</b>	Thawed	$\checkmark$	<b>~</b>	<b>~</b>	<b>✓</b>	<b>✓</b>		
	Fresh	<b>✓</b>	-	-	<b>✓</b>	-		
S4	Thawed	✓ ✓ ✓	<b>✓</b>	<b>/</b>	<b>✓</b>	-		
~-	Fresh	<b>✓</b>	<b>✓</b>	<b>~</b>	<b>✓</b>	<b>✓</b>		
<b>S5</b>	Thawed		<b>✓</b>	<b>✓</b>	<b>✓</b>	<b>✓</b>		
Q =	Fresh	<b>✓</b>	<b>✓</b>	<b>~</b>	<b>✓</b>	<b>✓</b>		
<b>S6</b>	Thawed	✓ ✓ ✓	<b>✓</b>	<b>✓</b>	<b>✓</b>	✓ ✓ ✓		
g <b>-</b>	Fresh	<b>✓</b>	<b>/</b>	<b>/</b>	<b>✓</b>	<b>✓</b>		
S7	Thawed	<b>✓</b>	<b>✓</b>	<b>✓</b>	<b>✓</b>	<b>✓</b>		
	Fresh	<b>✓</b>	-	-	<b>✓</b>	<b>✓</b>		
S8	Fixed	<b>✓</b>	-	-	-	<b>✓</b>		
	Fresh	✓ ✓ ✓	<b>✓</b>	<b>~</b>	<b>✓</b>	-		
S9	Fixed		<b>✓</b>	<b>/</b>	<b>✓</b>	-		
<b>.</b>	Fresh	<b>✓</b>	<b>✓</b>	<b>~</b>	<b>✓</b>	<b>✓</b>		
S10	Fixed	\ \ \ \	<b>✓</b>	<b>/</b>	<b>✓</b>	<b>✓</b>		
<b>a.</b> .	Fresh	<b>✓</b>	<b>~</b>		<b>✓</b>	<b>✓</b>		
S11	Fixed	<b>✓</b>	<b>✓</b>	<b>✓</b>	<b>✓</b>	<b>✓</b>		
S12	Fresh	<b>✓</b>	<b>✓</b>	<b>✓</b>	<b>✓</b>	-		
	Fixed	<b>✓</b>	<b>✓</b>	<b>✓</b>	<b>✓</b>	-		
S13	Fresh	-	-	-	-	-		
	Fixed	<b>✓</b>	<b>✓</b>	<b>✓</b>	<b>✓</b>	-		
S14	Fresh	<b>✓</b>	<b>✓</b>	<b>✓</b>	<b>✓</b>	-		
	Fixed	<b>✓</b>	<b>✓</b>	<b>/</b>	<b>✓</b>	-		

Quantitative MRI and histology metrics that we had for each sample. Some samples are missing certain scans or did not get sent for histological processing. For example, we do not have MTR or  $F_{\rm sat}$  data for the fresh version of S4, nor do we have histology data for this sample.

## S2 | OFF-RESONANCE RF SATURATION MAGNETIZATION TRANSFER THEORY

Below outlines some extra information about the off-resonance RF saturation magnetization transfer (MT) signal model that was fit  $^{30,31,52}$ . The water proton magnetization under steady-state RF saturation in a system with a free water proton pool  $M_{\rm f}$  and macromolecular proton pool  $M_{\rm m}$  is given by

$$\frac{M_{\text{sat,f}}}{M_{0,f}} = \frac{R\left(R_{1,f} + FR_{1,m}\right) + R_{1,f}\left(R_{1,m} + R_{\text{RF,m}}\right)}{\left(R_{1,f} + R_{\text{RF,f}}\right)\left(R_{1,m} + R_{\text{RF,m}}\right) + R\left(R_{1,f} + R_{\text{RF,f}} + F\left(R_{1,m} + R_{\text{RF,m}}\right)\right)}$$
(S1)

where  $\frac{M_{\text{sat,f}}}{M_{0,f}}$  is the ratio of the free water pool magnetization with and without RF saturation,  $R_{1,f}$  and  $R_{1,m}$  and are the rates of free water and macromolecular proton longitudinal relaxation, R is the cross-relaxation rate, F is the ratio of macromolecular protons to water protons, and  $R_{\text{RF,f}}$  and  $R_{\text{RF,m}}$  are the rates of RF saturation of the free and macromolecular proton pools given by:

$$R_{\rm RF,p}(\omega_1, \Delta) = \omega_1^2 g_{\rm p}(\Delta) \tag{S2}$$

where  $\omega_1 = \gamma B_1$  is the RMS amplitude of the applied saturation RF,  $\Delta$  is the applied RF frequency in Hz, and  $g_p(\Delta)$  is the normalized line shape for pool p (p=f or p=m). The free water pool is given by a Lorentzian function:

$$g_{\rm f}(2\pi\Delta) = \frac{T_{\rm 2,f}}{1 + (2\pi\Delta T_{\rm 2,f})^2}$$
 (S3)

and the macromolecular pool is given by a super-Lorentzian function  $^{53,54,55}$ :

$$g_{\rm m}(2\pi\Delta) = \pi\sqrt{\frac{2}{\pi}}T_{2,\rm m}\int_{0}^{1} \frac{1}{|3u^2 - 1|} \exp\left(-2\left(\frac{2\pi(\Delta - \Delta_{\rm cs,m})T_{2,\rm m}}{3u^2 - 1}\right)^2\right) du \tag{S4}$$

where  $T_{2,\mathrm{f}}$  and  $T_{2,\mathrm{m}}$  are the water proton and macromolecular proton  $T_2$  values and  $\Delta_{\mathrm{cs,m}}$  is the chemical shift in Hz between the water and macromolecular protons.

The parameters R,  $T_{2,m}$ , F (referred to as  $F_{\rm sat}$  in the main text), and  $\Delta_{\rm cs,m}$  were fit on a voxel-by-voxel basis.  $R_{1,\rm f}$  was set to 0.33  $s^{-1.46}$ ,  $R_{1,\rm m}$  was set to 1  $s^{-1.31,46,56}$ , and  $T_{2,\rm f}$  was set to a weighted average of the MWI  $T_2$  spectrum data for all  $T_2$  values beyond the 20 ms cutoff as discussed in the manuscript.  $\Delta$  and  $\omega_1$  were adjusted by  $B_0$  and  $B_1$  mapping on a voxel-by-voxel basis.

# S3 + SELECTIVE INVERSION RECOVERY $F_{SIR}$ PARAMETER CALCULATION

We model the bi-exponential behavior of the inversion recovery  $T_1$  mapping data as:

$$\frac{M_{\rm f}(t)}{M_{\rm for}} = a_{\rm fast}(1 - 2\exp(-R_1^+ t)) + a_{\rm slow}(1 - 2\exp(-R_1^- t)) \tag{S5}$$

where  $M_{\rm f}(t)$  is the longitudinal magnetization of the mobile protons at time t,  $M_{\rm f\infty}$  is its equilibrium value,  $R_1^-$  is the slow recovery rate,  $R_1^+$  is the fast recovery rate, and  $a_{\rm slow}$  and  $a_{\rm fast}$  are their corresponding amplitudes ( $a_{\rm slow} + a_{\rm fast} = 1$ ). We calculate a short  $T_1$  fraction map (short  $T_1$  F) from the fitted amplitudes as:  $\frac{a_{\rm fast}}{a_{\rm fast} + a_{\rm slow}} = a_{\rm fast}^{37}$ .

Setting  $b_{\rm f}^+ = -2 \, a_{\rm fast}$  and  $b_{\rm f}^- = -2 \, a_{\rm slow}$ , (S5) can be rewritten in the form of Equation 3 in Gochberg and Gore's paper <sup>41</sup>:

$$\frac{M_{\rm f}(t)}{M_{\rm f\infty}} = b_{\rm f}^{+} \exp(-R_1^{+}t) + b_{\rm f}^{-} \exp(-R_1^{-}t) + 1 \tag{S6}$$

The ratio of macromolecular to free water protons can be calculated using the formulation in Gochberg and Gore's paper <sup>41</sup>. We rewrite Equation 6 from Gochberg and Gore's paper using our paper's notation:

$$-2 a_{\text{fast}} = \left(\frac{M_{\text{f}}(0)}{M_{\text{f}\infty}} - \frac{M_{\text{m}}(0)}{M_{\text{m}\infty}}\right) \left(\frac{p_{\text{m}}}{p_{\text{f}}}\right)$$
 (S7)

where  $M_{\rm m}(t)$  is the longitudinal magnetization of the macromolecular protons at time t,  $M_{\rm m\infty}$  is its equilibrium value, and  $p_{\rm m}$  and  $p_{\rm f}$  are the sizes of the macromolecular and free water proton pools. Solving for the ratio of macromolecular to free water protons  $\frac{p_{\rm m}}{p_{\rm f}}$  (referred to as  $F_{\rm SIR}$  in the main text and as the pool size ratio (PSR) by Gochberg and Gore), we get:

$$F_{SIR} = \frac{-2 a_{fast}}{\left(\frac{M_f(0)}{M_{fighton}} - \frac{M_{im}(0)}{M_{mighton}}\right)}$$
(S8)

It follows from (S6) that the ratio  $\frac{M_{\rm f}(0)}{M_{\rm f\infty}}=-1$ . The hyperbolic secant pulse nearly saturates the macromolecular pool, which makes the ratio  $\frac{M_{\rm m}(0)}{M_{\rm m\infty}}\approx 0$ . Under these conditions and approximations,

$$F_{SIR,sech} \approx 2 a_{fast}$$
 (S9)

Using a Gaussian lineshape and T<sub>2</sub> between 10-20 µs for the macromolecular pool would cause  $\frac{M_m(0)}{M_{\rm m\infty}}$  to be  $\approx 0.88$  according to Gochberg and Gore <sup>41,42</sup>. Under these conditions and approximations,

$$F_{SIRgauss} \approx \frac{2 a_{fast}}{1.88} \approx 1.06 a_{fast}$$
 (S10)

Gochberg and Gore also state that in the case where the macromolecular pool was saturated by the inversion pulse, the PSR values would increase by a factor of  $\sim 1.91^{41,42}$ . Thus,

$$F_{SIRsech} \approx 1.91 F_{SIRgauss} \approx 1.91 (1.06 a_{fast}) \approx 2.02 a_{fast}$$
, (S11)

which is consistent with (S9).

# S4 | COMPARISON OF HYPERBOLIC SECANT VS. GAUSSIAN INVERSION PULSES

Our inversion recovery experiments utilized a high power (51  $\mu$ T) hyperbolic secant pulse<sup>57</sup> that nearly saturated the macromolecular pool, reducing the fast relaxing component amplitude. Based on the calculations in Section S3, in this case  $F_{SIR}$  would be approximately  $2\times$  the fast relaxing component amplitude.

We scanned one thawed sample with two inversion recovery sequences, one with a 51  $\mu$ T, 4000  $\mu$ s hyperbolic secant pulse and another with a 7.3  $\mu$ T, 4000  $\mu$ s Gaussian pulse and show the results below. The T<sub>1</sub> long and T<sub>1</sub> short maps do not significantly change depending on the choice of pulse, but their corresponding amplitude maps do. The T<sub>1</sub> short amplitude map ( $a_{\text{fast}}$ ) for the Gaussian pulse is about 2× that of the hyperbolic secant pulse. Their corresponding F<sub>SIR</sub> maps are consistent with one another and overall with literature values <sup>44,43,45,61</sup>, suggesting that the type of pulse used affects the F<sub>SIR</sub> parameter less than it affects the short amplitude.

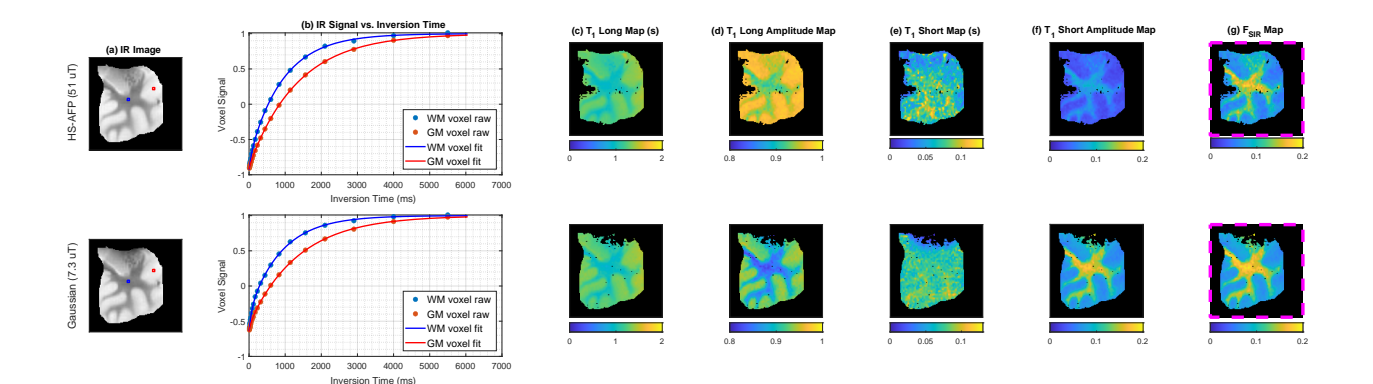


**FIGURE S3** Comparison of hyperbolic secant and Gaussian inversion pulses. (a) IR images (TI = 10 ms) for data collected with the the hyperbolic secant (HS) adiabatic full passage (AFP) inversion pulse <sup>57</sup> and Gaussian inversion pulse. (b) Observed and fitted signal recovery curves vs. inversion time for one WM voxel and one GM voxel in the ROI. (c) Map of the estimated long  $T_1$  value for each voxel. (d) Normalized corresponding signal amplitude for the long  $T_1$  component ( $a_{\text{slow}}$ ) for each voxel. (e) Map of the estimated short  $T_1$  value for each voxel. (f) Normalized corresponding signal amplitude for the short  $T_1$  component ( $a_{\text{fast}}$ ) for each voxel. (g)  $F_{\text{SIR}}$  map.

#### S5 + ADDITIONAL MYELIN-SENSITIVE PARAMETER: MTSAT

MTsat is another parameter that is sensitive to myelin content with a reduced dependence on  $T_1^{64,65,66,67,68,69,70}$ . These data were added to the supporting information section rather than the main body because to generate these maps we had to generate  $T_1$  weighted (T1w) images through simulation since we did not collect this data.

MTsat maps were calculated using Equations 7-8 from Helms et al  $^{64}$ . The MT weighted (MTw) images acquired at 10 kHz off-resonance and 8.8  $\mu$ T were used, and the corresponding images acquired at 60 kHz off-resonance were used as the proton density weighted (PDw) images. Apparent R<sub>1</sub> (R<sub>1app</sub>) maps were set to  $\frac{1}{T_1 \text{Long}}$  estimated in the biexponential T<sub>1</sub> fitting procedure, and A<sub>app</sub> maps were calculated using Equation 7b from Helms et al  $^{64}$ . Measured B<sub>1</sub> maps were incorporated according to Equation 5 in Rahman et al  $^{65}$ . T1w images of each sample were simulated using TR = 10 ms, flip angle = 50°, our T<sub>1</sub> long map, and a proton density map simulated from the PDw image, its TR and flip angle, and our T<sub>1</sub> long map. Figure S4 shows MTsat and MTR maps for comparison for two representative samples. Figure S5 plots MTR and MTsat vs. LFB ROI values to examine their correlation.

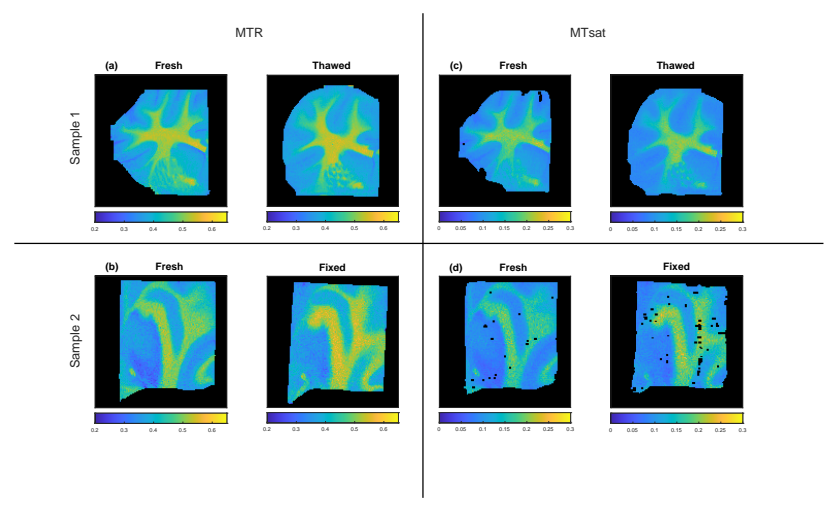


**FIGURE S4** MTR and MTsat maps for two representative samples including the fresh/thawed and fresh/fixed versions of each sample. (a) MTR maps from MT contrast images at average of -10kHz and 10kHz off-resonance and 8.8  $\mu$ T for fresh/thawed sample. (b) MTR maps for fresh/fixed sample. (c) MTsat maps generated as described above for fresh/thawed sample. (d) MTsat maps for fresh/fixed sample.

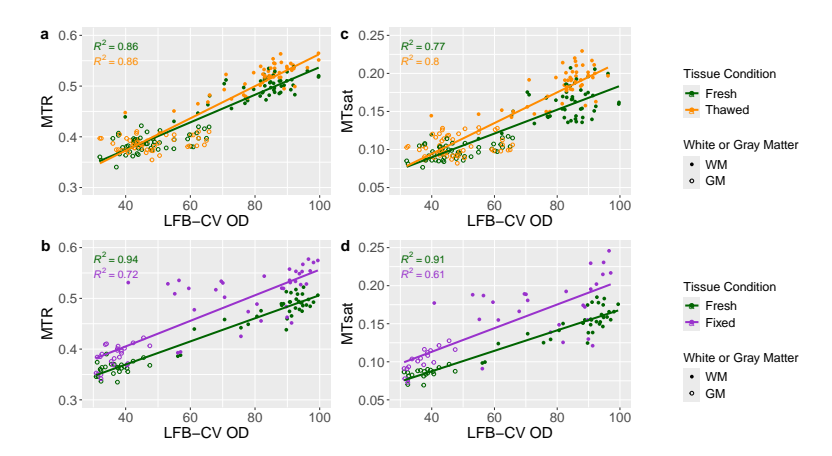


**FIGURE S5** Correlation between MTR and MTsat parameters and histology LFB-CV mean-adjusted values across tissue samples for fresh and thawed (Row 1) and fresh and fixed (Row 2) samples. Both MTR and MTsat a show strong correlation with LFB-CV OD for all ROIs as indicated by the high  $R^2$  values. MTsat exhibits a similar trend to the plots in Figure 7 in the main text based on the mixed-model analysis described in the methods section 2.5. (a-b) exhibit a statistically significant (p< 0.05) difference in slopes between the fresh/thawed fits (a: p = 0.022, b: p = 0.0039) and (c-d) exhibit a statistically significant (p < 0.05) difference in intercepts between the fresh/fixed fits (c: p = 0.033, d: p= 0.028).